# Ultrafast anisotropic phase separation governing photoinduced phase stability in submicron $Ti_3O_5$ crystals: Supporting Information

Ritwika Mandal[1, 2], Maciej Lorenc[1*], Marco Cammarata[3], Matteo Levantino[3], Serhane Zerdane[3, 4], Étienne Janod[2], Laurent Cario[2], Hiroko Tokoro[5, 6], Shin-ichi Ohkoshi[5], Elzbieta Trzop[1], Marina Servol[1], Guénolé Huitric[1,7], Hervé Cailleau[1], Vinh Ta Phuoc[8], Florian Banhart[9], Cristian Enachescu[10], Laurentiu Stoleriu[10], and Céline Mariette[3*]

[1*]Institut de Physique de Rennes, Université de Rennes, 263 avenue du Général Leclerc, Rennes 35042, France

[2]Institut des matériaux de Nantes Jean Rouxel (IMN), Nantes Université, CNRS, Nantes 44000, France

[3*]European Synchrotron Radiation Facility, 71 avenue des Martyrs, Grenoble 38043, France

[4]Paul Scherrer Institute (PSI), Forschungsstrasse 111, Villigen 5232, Switzerland

[5]Department of Chemistry, School of Science, The University of Tokyo, Bunkyo-ku, Tokyo, Japan

[6]Department of Materials Science, Faculty of Pure and Applied Sciences, University of Tsukuba, Tsukuba, Ibaraki, Japan

[7]Laboratoire des Solides Irradiés, CEA/DRF/lRAMIS, Ecole Polytechnique, CNRS, Institut Polytechnique de Paris, Palaiseau 91128, France

[8]GREMAN—UMR 7347 CNRS, Université de Tours, 60 Rue du Plat d'Étain, Tours 37000, France

[9]Institut de Physique et Chimie des Matériaux, UMR 7504, Université de Strasbourg, 23 rue du Loess, Strasbourg 67034, France

[10]Faculty of Physics, Alexandru Ioan Cuza University, Bulevardul Carol I 11, Iasi 700506, Romania

# 1 Surface Morphology of $Ti_3O_5$ pellets

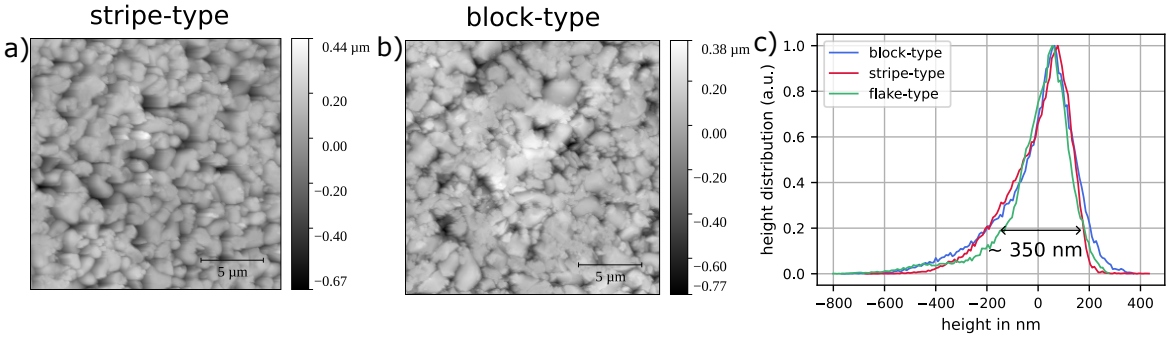


Figure 1: **Atomic Force Microscopy(AFM) images of the pellets** a) and b) AFM height images of 20 × 20 $\mu m^2$ regions on the surface of the a) stripe type and b) block type $Ti_3O_5$ pellets. c) Height distribution extracted from AFM images. The standard deviation of the height distribution indicates similar surface roughness for each of them ($\sim$ 350 nm). The height distribution of the flake type pellet has been reproduced from Supplementary Information [1]

[1] Mariette, C. et al. Strain wave pathway to semiconductor-to-metal transition revealed by time-resolved X-ray powder diffraction. Nature Communications 12, 1239. issn: 2041-1723. https: //doi.org/10.1038/s41467-021-21316-y (Feb. 2021).

## 2 Effect of excitation laser wavelength on the thermal transformation peak

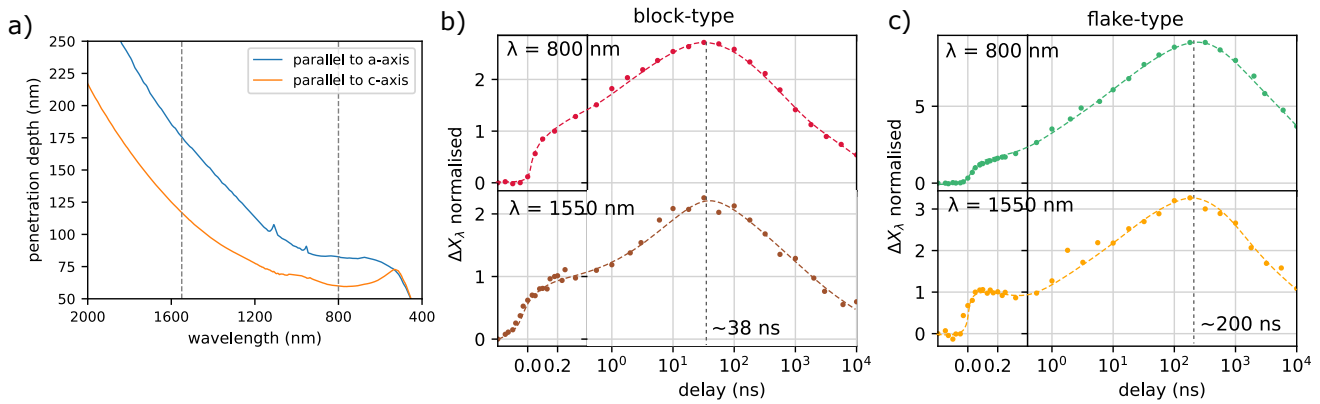


Figure 2: a) The penetration depth of the pump laser as a function of the wavelength calculated from the imaginary component of the refractive index measured for a single crystal of $Ti_3O_5$ along different lattice axes, ***a*** (blue curve) and ***c*** (orange curve). The penetration depth along ***a*** or ***c*** axis for wavelength 1550 nm has a mean value of 150 nm which is approximately twice than that for wavelength of 800 nm with a mean depth of 70 nm (see dashed lines). The percentage of $\lambda$-phase fraction ($\Delta X_\lambda$) is plotted for b) the block type $Ti_3O_5$ and c) the flake type pellet at two different pump wavelengths namely, 800 nm (top) and 1550 nm (bottom). $\Delta X_\lambda$ values are normalised to their value at 200 ps. The dotted grey vertical lines indicate the maximum transformation that occurs at the same delay for the two wavelengths both for block type and flake type.

## 3 Effect of incidence laser fluence on the thermal transition peak

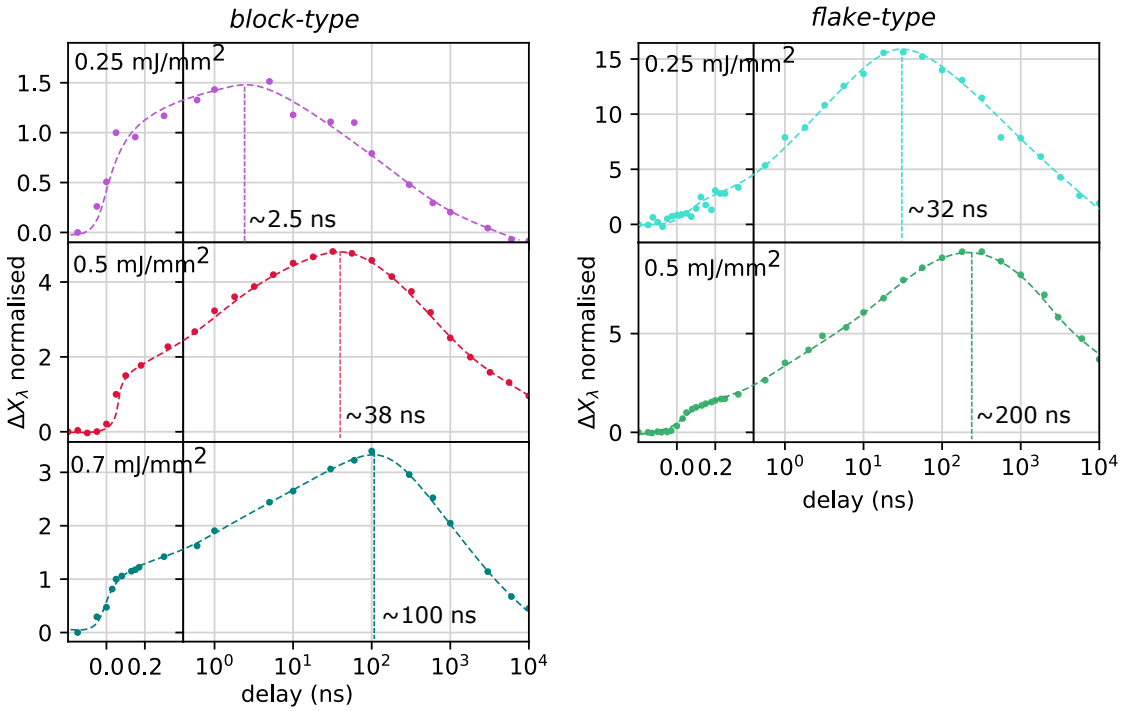


Figure 3: Time evolution of the change of the $\lambda$-phase fraction ($\Delta X_\lambda$), normalised to the value at 100 ps. $\Delta X_\lambda$ are obtained from the Rietveld refinement of the time-resolved powder patterns measured for the block type (left) and the flake type (right) at different laser fluences.

# 4 Heat diffusion model: Results based on different initial conditions:

Different initial conditions with various sets of thermal exchange coefficients have been tested for the heat diffusion model as mentioned in the article. The simulation parameters used here are summarized in the table below:

Table 1: Parameters used for the simulations; where x,y can be either $\lambda$ or $\beta$ phase.

| coefficient | value |
|---|---|
| $c_{i,i}^{\lambda\lambda}$ | 2e-9 |
| $c_{i,i}^{\beta\beta}$ | 4e-9 |
| $c_{i,i}^{\beta\lambda} = c_{i,i}^{\lambda\beta}$ | 1.3e-9 |
| $B = \frac{c_{i,j}^{xy}}{c_{i,i}^{xy}}$ | 10 |
| $c_{i,bulk}^{\beta}$ | 4e-12 |
| $c_{i,air}^{\beta}$ | 2.5e-15 |
| $T_S$ | 2500 K |
| System size | $500 \times 500$ nodes |
| Nb of switched nodes | 1200 nodes |

## 4.1 Excitation of whole grains within the first layer of grains

In this case, we assume that upon the strain propagation, there can be a collective excitation of the whole crystallite. The temperature distribution on the $\lambda$-nodes within a crystallite follows an exponential decrease in depth with a surface temperature of 2500 K. The temperature profiles on the $\lambda$ node for different grainsizes have been shown in Fig. 4c.

For any set of parameters chosen, we see that the relative peak shift is such that the bigger crystallite relaxes later than the smaller crystallite. This trend is opposite to that have been observed in the experimental data.

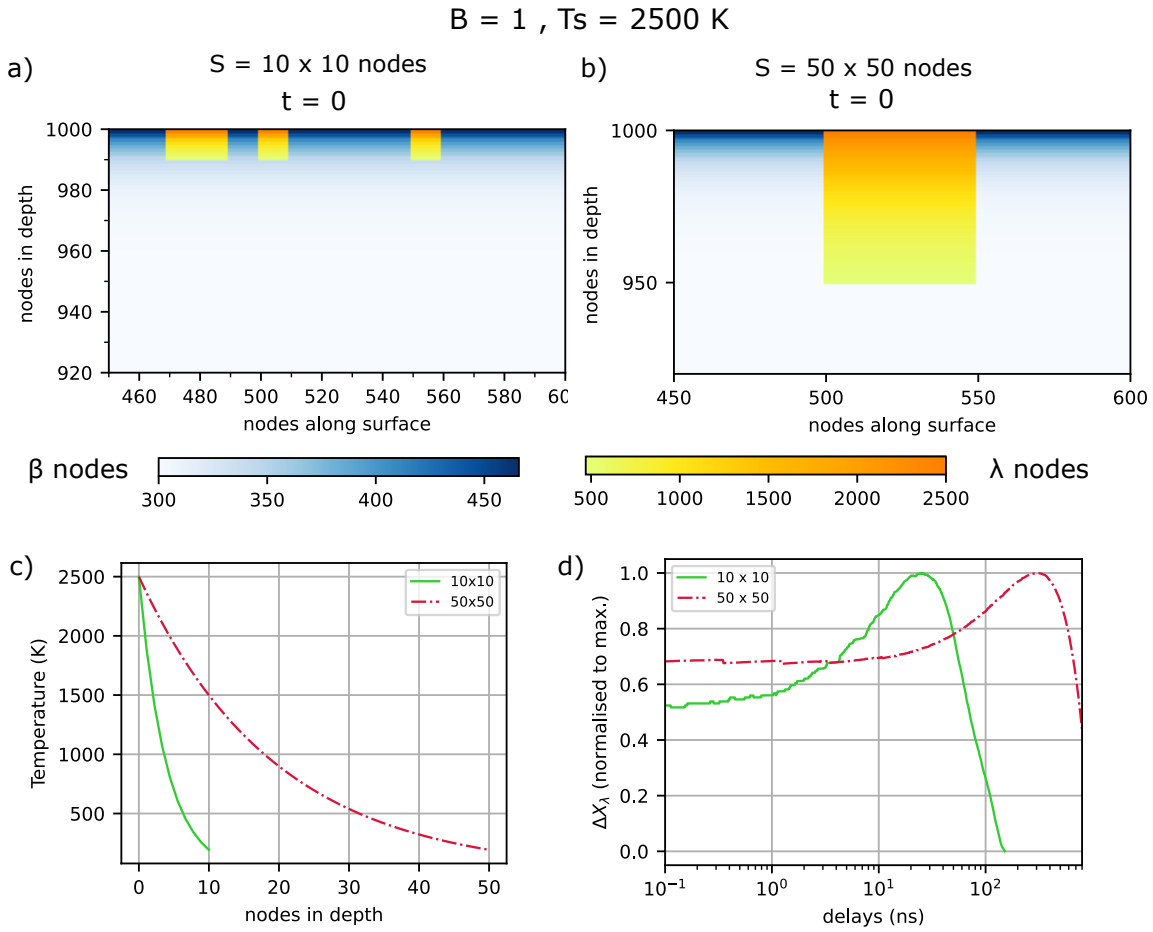


Figure 4: Spatial distribution of the $\lambda$ and $\beta$-phases at the initial state for grainsizes a) S = 10 $\times$ 10 and b) 50 $\times$ 50 nodes. c) The temperature profile with depth in S = 10$\times$10 and S = 50$\times$50 nodes. d) The evolution of the $\lambda$-phase fraction with delays. The coefficient B = 1 and other coefficients like $c_{i,air}$ and $c_{i,bulk}$ have the same values as in Table 1. The fraction is normalised to the maximum value to compare the peak shift only.

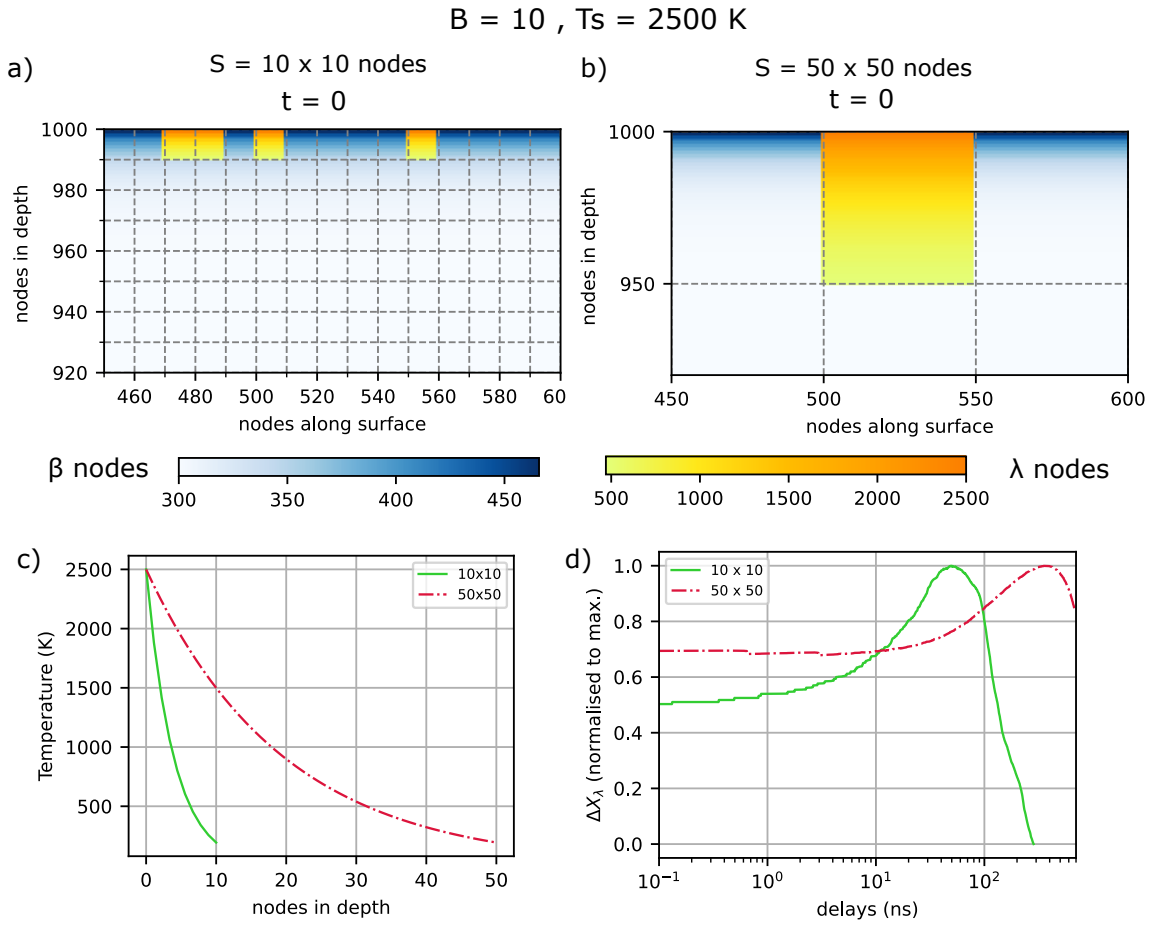


Figure 5: Spatial distribution of the $\lambda$ and $\beta$-phases at the initial state for the grains sizes a) S = 10×10 and b) S = 50×50 nodes respectively. The dashed lines indicate the grain boundaries. c) The temperature profile with depth in S = 10×10 and S = 50×50 nodes d) The evolution of the $\lambda$-phase fraction for both the grain sizes with delays. The fraction is normalised to the maximum value to compare the peak shift only.

## 4.2 Excitation in the form of domains below the photoexcited surface but limited by laser penetration depth

The initial pattern assumes an excitation of an entire crystallite below the surface with a limitation in depth by the laser penetration. The temperature distribution on the strain transformed $\lambda$-nodes within a crystallite follows an exponential decrease in depth with a surface temperature of 2500 K and is same for both the smaller and bigger crystallites.

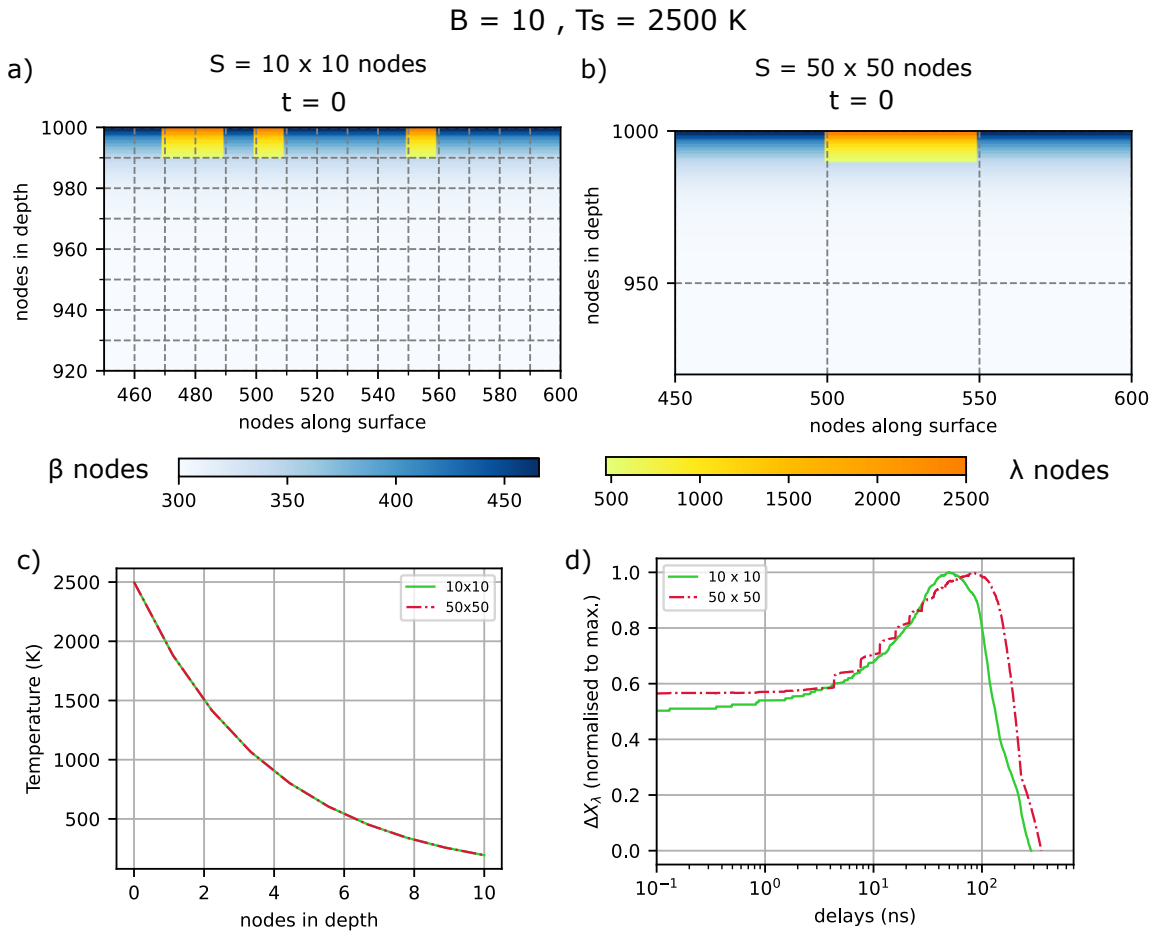


Figure 6: a) and b) Spatial distribution of the $\lambda$ and $\beta$ phases at the initial state for the grains sizes 10×10 and 50×50 respectively. c) The temperature profile on the $\lambda$ nodes at the initial state. The same profile is used for both grain sizes. d) The evolution of the $\lambda$ phase fraction (normalised to the maximum value) for both grain sizes with delays.

# 5 Heat diffusion model: Effect of latent heat

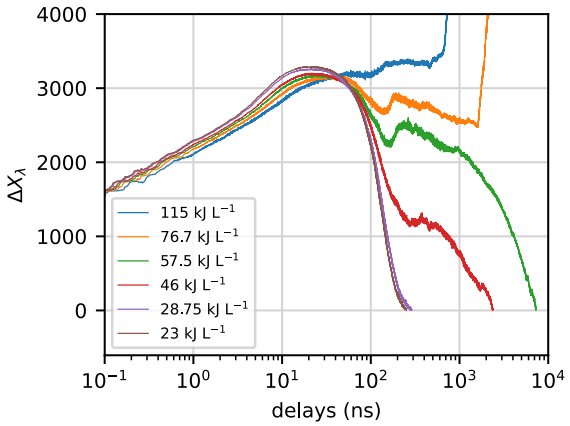


Figure 7: Evolution of the $\lambda$ phase fraction for simulations taking into account different latent heat values.